MATERIALS SCIENCE

Controlled generation of luminescent centers in hexagonal boron nitride by irradiation engineering

M. Fischer[1,2,3], J. M. Caridad[2,4,5], A. Sajid[4], S. Ghaderzadeh[6], M. Ghorbani-Asl[6], L. Gammelgaard[2,4], P. Bøggild[2,4], K. S. Thygesen[2,4], A. V. Krasheninnikov[6,7], S. Xiao[1,2,3], M. Wubs[1,2,3], N. Stenger[1,2,3]*

Luminescent centers in the two-dimensional material hexagonal boron nitride have the potential to enable quantum applications at room temperature. To be used for applications, it is crucial to generate these centers in a controlled manner and to identify their microscopic nature. Here, we present a method inspired by irradiation engineering with oxygen atoms. We systematically explore the influence of the kinetic energy and the irradiation fluence on the generation of luminescent centers. We find modifications of their density for both parameters, while a fivefold enhancement is observed with increasing fluence. Molecular dynamics simulations clarify the generation mechanism of these centers and their microscopic nature. We infer that V_NC_B and V_B^- are the most likely centers formed. Ab initio calculations of their optical properties show excellent agreement with our experiments. Our methodology generates quantum emitters in a controlled manner and provides insights into their microscopic nature.

INTRODUCTION

Quantum emitters are the cornerstones of many applications such as quantum telecommunication (*1*), quantum sensing (*2*), and quantum metrology (*3*). Therefore, quantum emitters in solid-state systems such as semiconductor quantum dots (*4*), nitrogen-vacancy (*5*), and silicon-vacancy (*6*) centers in diamond have become rapidly growing research fields. Recent experiments at cryogenic temperatures have demonstrated that two-dimensional (2D) materials can host quantum emitters (*7*–*9*) even with site selectivity on the submicrometer scale (*10*). Achieving site-selective and on-demand quantum emitters (*11*) at room temperature is an experimental challenge. Achieving this would be useful to mature emerging technologies such as quantum computing and communications (*12*) without cryogenic cooling systems.

The 2D material hexagonal boron nitride (hBN) can host luminescent centers deep within the large, indirect bandgap of ~6 eV (*13*). These centers showed room temperature quantum emission (*14*) making hBN a promising platform to achieve site-selective quantum emitters at room temperature. The 2D nature of hBN enables placing quantum emitters in close proximity to optical cavities (*15*) and coupling of quantum emitters to plasmonic structures (*16*) for optimized light-matter interactions (*11*, *17*). Recent studies show complex photophysics of quantum emitters (*18*) as well as multiple-emitter contributions (*19*). The origin of these luminescent centers is ascribed to several defects in the hBN lattice (*20*–*22*), but their microscopic nature is still under debate because the generation mechanism remains poorly understood.

Except for bottom-up techniques such as chemical vapor deposition, at least one further method is required to generate quantum emitters in hBN. The most commonly used method is to dropcast a solution of low-quality hBN flakes on a substrate followed by thermal annealing in argon at 850 °C (*23*). Hereby, usually low-quality hBN flakes are used, which are known to host many intrinsic defects. This was manifested by the fact that standard furnace annealing generated a large number of luminescent centers in this low-quality hBN, while it was less efficient for high-quality hBN (*24*). Starting with fewer defects enables a highly controlled generation of quantum emitters required for applications in quantum photonics (*12*).

Besides thermal annealing of hBN of various qualities, oxygen plasma (*24*, *25*) and high-energy oxygen irradiation (*26*, *27*) have been used to generate quantum emitters in hBN. However, applying irradiation engineering, i.e., tuning both irradiation energy and irradiation fluence (defined as the number of atoms per area), remains unexplored on hBN, while this technique can create defects controllably in other 2D materials (*28*).

Here, we present a novel method to enhance the generation of luminescent centers in hBN via irradiation engineering with oxygen atoms and subsequent annealing. We tune the irradiation energy from 120 to 300 eV as well as the irradiation fluence by a factor of 10 to controllably generate luminescent centers in high-quality hBN with few intrinsic defects. We find a maximum density of luminescent centers at 240 eV and a remarkable, fivefold enhancement when increasing the irradiation fluence by 10. Furthermore, several of these luminescent centers are confirmed to be quantum emitters.

The results of our irradiation engineering in combination with molecular dynamics (MD) simulations strongly suggest that irradiation-induced amorphization followed by recrystallization creates two groups of luminescent centers in the topmost layers. Furthermore, we demonstrate that irradiation with oxygen atoms controls the density of generated luminescent centers in hBN. The presented method is wafer-scalable and could be extended to other gapped 2D materials as well as other irradiating atoms or ions. Our experimental and theoretical findings indicate that the two groups of luminescent centers are related to V_NC_B and V_B^- defects, as evident in particular from an excellent agreement of the experimental photoluminescence (PL) line shapes with the results of ab initio calculations.

---

[1]Department of Photonics Engineering, Technical University of Denmark, 2800 Kgs. Lyngby, Denmark. [2]Center for Nanostructured Graphene, Technical University of Denmark, 2800 Kgs. Lyngby, Denmark. [3]NanoPhoton - Center for Nanophotonics, Technical University of Denmark, 2800 Kgs. Lyngby, Denmark. [4]Department of Physics, Technical University of Denmark, 2800 Kgs. Lynby, Denmark. [5]Department of Physics and NanoLund, Lund University, box 118, 22100 Lund, Sweden. [6]Institute of Ion Beam Physics and Materials Research, Helmholtz-Zentrum Dresden-Rossendorf, 01328 Dresden, Germany. [7]Department of Applied Physics, Aalto University, 00076 Espoo, Finland.
*Corresponding author. Email: niste@fotonik.dtu.dk

RESULTS AND DISCUSSION

Generation of luminescent centers in hBN

Our irradiation-based generation process is illustrated in Fig. 1A. We mechanically exfoliate high-quality hBN flakes onto SiO_2/Si substrates. The samples are subsequently irradiated with oxygen atoms at controlled kinetic energies between 120 and 300 eV in a reactive ion etch (RIE) reactor where the irradiation fluence is selected by the irradiation time. Here, the oxygen atoms are mostly neutral with a small fraction of positively charged oxygen (see Materials and Methods). This irradiation is carried out at low pressure providing a narrow energy distribution as well as a small angular dispersion (*29*). After irradiation, the samples are annealed at 850 °C in nitrogen (details in Materials and Methods). We monitor the evolution of the optical properties of our samples during the generation process by a customized confocal microscope with a lateral resolution of 1 μm (see Materials and Methods and section SI). All spectra shown in this work are not background-corrected. We take 0.5-μm-grid PL maps after each step of our generation process (Fig. 1B). Unnormalized PL maps are shown in section SII.

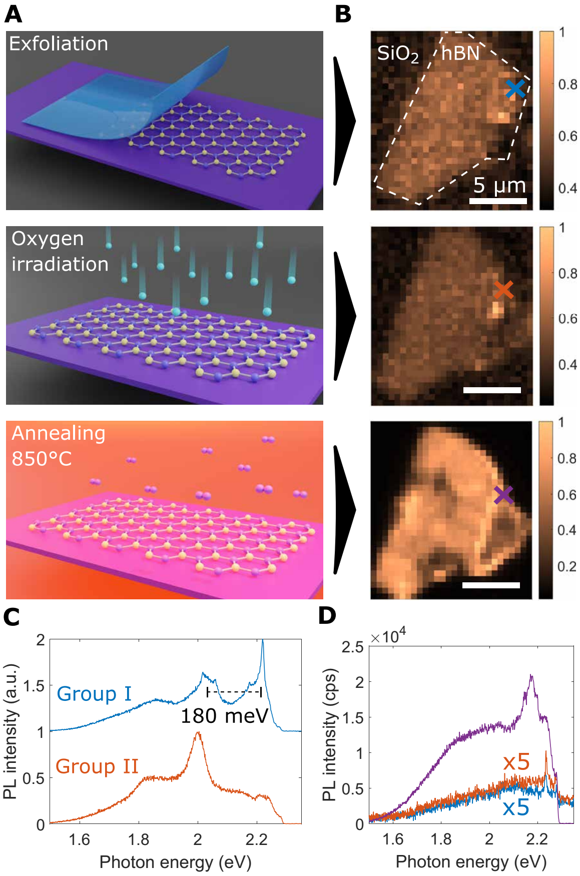

Fig. 1. Process of luminescent center generation in hexagonal boron nitride by irradiation engineering. (**A**) Schematic of the three fabrication steps for generating luminescent centers in hBN: mechanical exfoliation, irradiation with oxygen atoms, and thermal annealing in nitrogen. (**B**) PL maps after each fabrication step showing the evolution of one hBN flake. The color scales show the integrated PL counts normalized to each map. (**C**) Typical spectra of luminescent centers of group I and group II. a.u., arbitrary units. (**D**) Spectral evolution of an individual luminescent center. Each spectrum is given in counts per second (cps), and the colors of the spectra correspond to the colors of the crosses in (B). The spectra after exfoliation and pure irradiation are multiplied by 5. All data shown are obtained from hBN flakes of batch 1 irradiated for 10 s at 240 eV.

By taking PL maps after each step, the evolution of individual luminescent centers is monitored. A typical evolution of one luminescent center is shown in Fig. 1D. After exfoliation, a flat PL spectrum is observed (blue curve), indicating no luminescent center. The sharp peak at 2.235 eV is the Raman-active E_{2g} phonon in hBN (*30*) for a 2.37-eV excitation laser (see Materials and Methods). The PL spectrum remains unchanged after irradiation, but a clear PL peak around 2.17 eV appears after subsequent annealing. This luminescent center appeared at the edge of the flake, although other centers appeared away from the edge (see section SIII). Both irradiation and annealing are crucial steps to achieve many luminescent centers per area, as discussed below.

Luminescent centers generated by our process can be classified into two main groups depending on the shape and intensity of their zero-phonon line (ZPL) and phonon side bands (PSBs). Representative spectra of these groups of luminescent centers are shown in Fig. 1C, while more spectra are shown in section SIV. The first group (group I) is characterized by a narrow ZPL followed by two marked PSBs red-shifted by 160 to 200 meV from the ZPL, corresponding to phonon-assisted PL involving bulk optical phonons (*31*, *32*). We find a second group (group II) that displays a broader and less pronounced ZPL associated with a series of red-shifted, overlapping PSBs of acoustic and optical nature. These PSBs are less marked than in group I. We note that this classification of luminescent centers is specific to this work and cannot be directly compared to the nomenclature presented in previous studies (*23*, *33*).

Studying different irradiation energies and irradiation fluences

In our studies, we use three different bulk crystals for exfoliation of multiple hBN flakes resulting in three different batches (batches 1, 2, and 3), all from the same manufacturer (see Materials and Methods). To quantify the efficiency of generating luminescent centers in hBN, we define the density per unit surface

$$S = N/A$$

Here, N is the number of generated centers and A is the area of all hBN flakes. Details on the number of generated centers and the flake areas are given in section SV.

First, we focus on the density after each process step (Fig. 2A). For batch 1, we find no luminescent centers in untreated flakes after exfoliation and only few after irradiation. After subsequent annealing of batch 1, the density increases up to 0.012 centers/μm^2. For reference, we also investigate the density of batch 1 after annealing without prior irradiation and find a density of 0.005 centers/μm^2. Since this density is well below 0.012 centers/μm^2, both irradiation and annealing are crucial steps to achieve high densities. In contrast to batch 1, a small, nonzero density was observed in batch 2 before treatment. While both batches are from the same supplier and nominally comparable, batch 1 and batch 2 were taken from different crystals. Such differences in crystallinity and purity are typical between crystals. After irradiation of batch 2, the density decreases close to zero because most of the centers present after exfoliation do not withstand the irradiation. Subsequent annealing increases the density up to 0.028 centers/μm^2, which is higher than in batch 1. For both batches, the density is small after exfoliation because high-quality

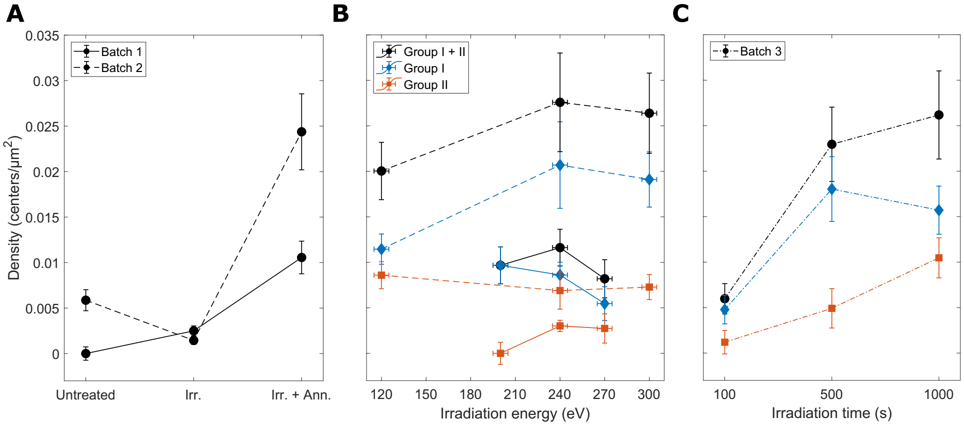

Fig. 2. Densities of luminescent centers. Group I centers are shown in blue, group II centers are in red, and the sum of both is in black. (**A**) Total densities of luminescent centers in untreated, after 10-s irradiation (Irr.), and subsequently annealed (Irr. + Ann.). (**B**) Densities for different irradiation energies after 10-s irradiation and subsequent annealing. (**C**) Density dependence on the irradiation time after 240-eV irradiation and subsequent annealing.

hBN is used with a low density of intrinsic luminescent centers (*24*). The density for individual irradiation energies after each process step is shown in section SVI. For both batch 1 and batch 2, a maximal density is observed after irradiation and subsequent annealing (Fig. 2A). Thus, both irradiation and thermal annealing are crucial steps to obtain high densities of luminescent centers in hBN.

Second, we study the density as a function of irradiation energy. By fine-tuning the bias voltage of our RIE reactor, we can choose irradiation energies from 120 to 300 eV with a precision of ±5 eV (see Materials and Methods). This relatively narrow energy resolution allows us to study the influence of the irradiation energy on the density with energy steps of a few tens of electron volts only. In Fig. 2B, the density is displayed for group I (red) and group II (blue) centers as well as the total density (black), for batches 1 and 2. For batch 1, we observe a maximum total density at 240 eV. Batch 2 shows a general increase of the total density with the irradiation energy followed by a slight decrease or a saturation after 240 eV. The measurement uncertainties (see section SVII) allow two interpretations: either a maximum total density at 240 eV or a linear increasing density with energy, as discussed below. For group I centers of batch 1, we observe a decrease in density with increasing energy, while batch 2 shows an increase similar to the total density. For both batches, the density for group II is inverted to the one of group I.

Besides tuning the irradiation energy, we can also tune the irradiation time while keeping the flux of oxygen atoms constant (see Materials and Methods). This allows us to tune the irradiation fluence and thus investigate the effect on the density of luminescent centers (Fig. 2C). A substantial, fivefold increase in total density is observed by increasing the fluence by 10. It appears that this enhancement is bigger for group I than for group II. The enormous enhancement with increasing fluence alters the density much stronger than tuning the irradiation energy. Thus, the mechanism of generating luminescent centers is dominated by the fluence, as discussed below.

Photophysical properties of luminescent centers

To analyze the photophysics of our luminescent centers, we choose the most stable emitters for intensity correlation measurements, also called $g^{(2)}$ measurements (see section SI). In Fig. 3A, PL spectra from localizing the centers and during the $g^{(2)}$ measurements are shown. These spectra show good agreement, and thus, only small spectral wandering is observed. We fit our experimental correlation functions with theoretical curves of a three-level system

$$g^{(2)}(\tau) = 1 - b \cdot e^{-|\tau|/T_1} + c \cdot e^{-|\tau|/T_2} \tag{1}$$

where b is the antibunching amplitude, c is the bunching amplitude, and T_1 and T_2 are the lifetimes of the antibunching and bunching process, respectively. By convoluting Eq. 1 with our instrument response function (see section SI), we obtain the antibunching dips given in Fig. 3B. For 240 eV, we measure the $g^{(2)}$ function of a PSB, which is a reliable test of the quantum nature of luminescent centers (*31*). A value of $g^{(2)}(0)$ below 0.5 means that the single-photon contribution is nonzero, but not necessarily high (*34*). For 200-eV irradiation, we find a luminescent center with $g^{(2)}(0) = 0.069 \pm 0.403$, indicating clear quantum emission. Further centers show $g^{(2)}(0) = 0.533 \pm 0.087$ and $g^{(2)}(0) = 0.876 \pm 0.149$ after 240 and 270 eV, respectively. More experimental data of extended $g^{(2)}$ functions and stability measurements are shown in section SIX.

MD simulations of oxygen irradiation

To get insights into the microscopic processes taking place under oxygen irradiation, we carried out MD simulations. We studied the irradiation with oxygen ions onto a six-layer hBN target under normal incidence (Fig. 4A and section SX). The average number of boron (V_B) and nitrogen vacancies (V_N) per incident oxygen atom was calculated for different irradiation energies (Fig. 4B and movies S1 and S2). The numbers of both V_B and V_N increase almost linearly with increasing irradiation energy while we obtained an overall higher number for V_N. This is in agreement with the lower formation energy of 7.3 eV for V_N compared to 10.4 eV for V_B reported by extended Tersoff potential (ExTeP) (*35*) and density functional theory (DFT) (*21*). This lower vacancy formation energy makes it easier to displace a nitrogen atom in the hBN lattice and to form V_N.

For two batches of hBN, our experiments showed a slight increase in the density of generated luminescent centers when increasing the irradiation energy from 120 to 240 eV and a slight decrease

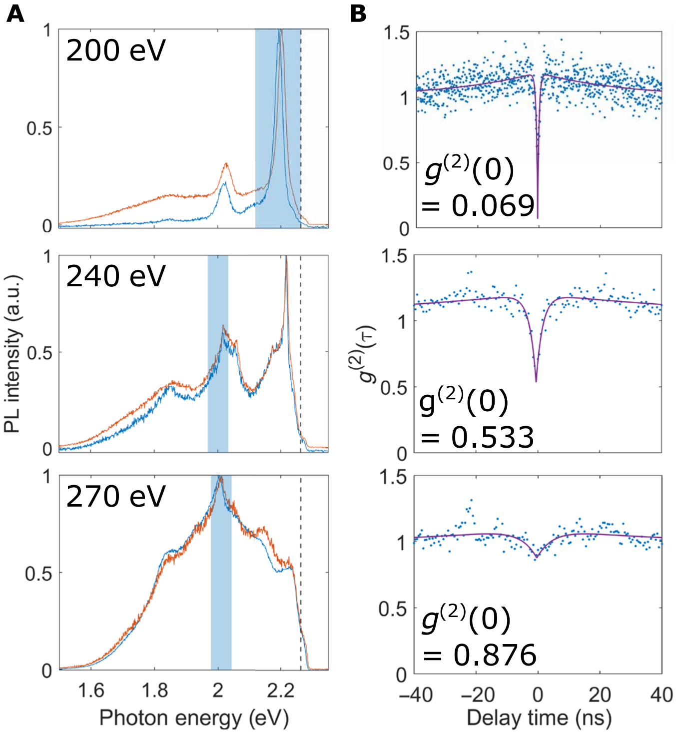

Fig. 3. Photophysics of luminescent centers. The luminescent centers shown are obtained after 10-s irradiation and annealing (batch 1). (**A**) The spectrum from localizing the centers (red) and during the $g^{(2)}$ measurement (blue) is shown. (**B**) The $g^{(2)}$ functions of selected emitters. The collected spectral region is shaded blue in (A). The corresponding irradiation energy is given by the inset text in (A). The fractions of ZPL emission are given in section SVIII.

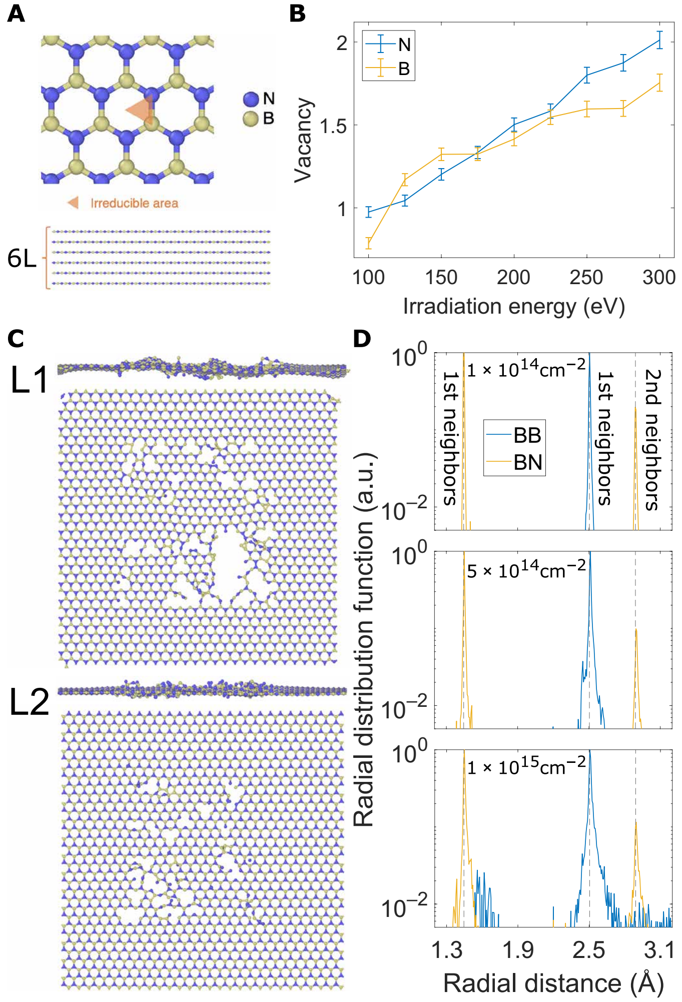

Fig. 4. MD simulations of oxygen irradiation of hBN. (**A**) Simulation setup for oxygen irradiation. (**B**) Average numbers of V_N and V_B produced at different irradiation energies. (**C**) Top and side views of amorphous hBN layers after high-fluence irradiation at 1×10^{15} cm^{-2}. The layers are obtained with 100-eV irradiation and subsequent annealing at 100 °C. L1 stands for the topmost layer; L2 stands for the second topmost layer. (**D**) Radial distribution functions of the three topmost layers after irradiation with different fluences at 100 eV and subsequent annealing at 100 °C. The boron-boron (BB) neighbors are shown in blue, the boron-nitrogen (BN) neighbors are shown in yellow, and the pristine system is shown in black dashed lines.

or saturation from 240 to 300 eV (see Fig. 2B). Within our measurement uncertainties, one valid interpretation is a linear increase of the density with irradiation energy. This linear increase is not as large as the vacancies concentration increase predicted by our MD simulations (see Fig. 4B). One possible reason is the annihilation of V_N by the subsequent annealing in nitrogen atmosphere via breaking nitrogen molecules (see section SXI). Another possible reason is that the empirical MD cannot differentiate between ions and atoms while we irradiate with a small contribution of positively charged oxygen (see section SXII).

As described above, we also experimentally studied the influence of the irradiation fluence on the density of generated luminescent centers in hBN. We observed a remarkable, fivefold enhancement in the density when increasing the fluence by a factor of 10. To get an understanding of this observation, we carried out MD simulations for high-fluence irradiation (see movies S3 and S4). An additional annealing at 100 °C was performed after ion impact simulations with the main goal to remove metastable configurations, but not to mimic the experimental annealing process, as macroscopic times cannot be achieved even in analytical potential MD simulations. In Fig. 4C the first two hBN layers after a fluence of 1×10^{15} cm^{-2} are shown. Both layers are very amorphous and show large distortions both in and out of plane. The third and fourth layers remain crystalline after irradiation with only slight deformation out of the plane (see section SX). To quantify the observed amorphization of hBN, we calculated the radial distribution function (RDF) for the top three layers of hBN (Fig. 4D). The RDFs were calculated for fluences from 1×10^{14} to 1×10^{15} cm^{-2}, which are around our experimental fluences (see Materials and Methods). The RDFs for a monocrystalline material are Dirac delta functions corresponding to constant atom-to-atom distances in the crystal (black dashed lines in Fig. 4D). After high-fluence irradiation, the first three hBN layers show broad peaks in the RDF, indicating an amorphous material. The boron-boron distance (blue curves in Fig. 4D) is a broad peak for a fluence of 1×10^{14} cm^{-2} and becomes even broader when increasing the fluence up to 1×10^{15} cm^{-2}. Hence, the higher the irradiation fluence, the more amorphous the hBN becomes, as expected from our experiments.

To get further insights into the optical properties of our amorphous hBN after irradiation, we analyzed the electronic structure of the top four irradiated layers (see section SXIII). Defects lead to important changes in the electronic structure of the two topmost layers by introducing a large number of midgap states. The defect-associated states cover the entire bandgap region and stem from both valence band and conduction band orbitals, as both types of elements are removed from the lattice. For the third and fourth layer, however, the electronic structure changes only slightly, while a few strongly localized states are obtained for the third layer.

The results of our experiments and MD simulations indicate strongly that amorphization of the two topmost layers takes place under irradiation with oxygen ions. Thus, we propose the following mechanism for the generation of luminescent centers in hBN. The irradiation amorphizes the topmost layers and erases luminescent centers previously present. This is supported by the experimental observation that luminescent centers present beforehand are erased after irradiation (see batch 2 in Fig. 2A). Thermal annealing recrystallizes the amorphous layers, so that a few defects remain in the topmost layers. The recrystallization is experimentally supported by bulk phonon-assisted PL (*31*, *32*) observed in group I emitters (see Fig. 1C). We note that the very amorphous topmost layer can also evaporate during thermal annealing and that the annealing step cannot be simulated by using MD, as macroscopic time scales cannot be achieved in practice.

DFT calculations of PL line shapes of defects

To get insights into the microscopic origin of our luminescent centers, we consider both the irradiation and annealing steps in our generation process (Fig. 1A). Irradiation with oxygen atoms forms V_B and V_N (see Fig. 4B) but can also create the double vacancy V_{BN} and oxygen atoms on nitrogen sites (O_N). Note that oxygen atoms on boron sites (O_B) are less likely (*36*). Subsequent annealing in a nitrogen environment provides nitrogen atoms (by breaking nitrogen molecules) leading to the annihilation of V_N and O_N as well as transforming V_{BN} into V_B (see section SXI). Thus, V_B is the only irradiation-induced defect withstanding annealing in nitrogen.

Besides irradiation-induced defects, impurities can be incorporated in the hBN lattice during our process (Fig. 1A). The carbon substitutes C_B and C_N can be incorporated into the hBN lattice from ubiquitous hydrocarbons (*37*). Since carbon is present in our experiments both intrinsically in the hBN and in the annealing environment (see Materials and Methods), C_B and C_N are likely to be formed.

All in all, we have V_B, C_B, and C_N formed during our process. During annealing, these defects become mobile and new defects can be formed; in particular, V_B and C_N can merge into V_NC_B. Theoretical investigations predict C_B and C_N to be optically inactive in our spectral regime (*38*). Furthermore, V_NC_B has been ascribed to quantum emission (*39*) and V_B^- (negatively charged V_B) has been ascribed to optically detected magnetic resonance (*40*, *41*). Therefore, we choose V_NC_B and V_B^- (Fig. 5A) to calculate PL line shapes via DFT.

Figure 5B shows the PL line shapes of V_NC_B and V_B^- obtained from DFT calculations (details in Materials and Methods and section SXIV). Pronounced PSBs are observed for V_NC_B, while the calculated spectrum of V_B^- shows a broad ZPL with less pronounced PSBs. In Fig. 5C we compare two representative luminescent centers of groups I and II (also shown in Fig. 1C) to the calculated spectra. This qualitative comparison is done by matching the ZPLs of experimental and calculated line shape. Furthermore, the calculated line shapes were rescaled in intensity such that the PSBs fall on top of each other. Excellent agreement of group I and V_NC_B as well as group II and V_B^- is found. A small deviation is that the calculated V_B^- spectrum vanishes above the ZPL, whereas the group II centers show a ZPL on top of a broad background. Possible reasons for deviations between calculated and experimental spectra are effects of edges, layers, material distortion, and strain on the luminescence properties of defects (*39*, *40*, *42*). Nevertheless, our excellent agreement outstands previously reported comparisons of experiments with ab initio calculations.

In this work, we have studied the generation of luminescent centers in hBN via an irradiation-based process. The versatile processes in our RIE reactor allow irradiation engineering by tuning both the irradiation energy and the irradiation fluence. This is novel compared to previous studies of high-energy irradiation (*26*, *27*) and oxygen plasma (*24*, *25*) processes, since highly directional ions with a narrow energy distribution were used in the present work. The density of generated luminescent centers changes with both irradiation energy and fluence, while increasing the irradiation fluence shows a substantial enhancement of the density. Within our luminescent centers, we find two groups, named groups I and II, which show

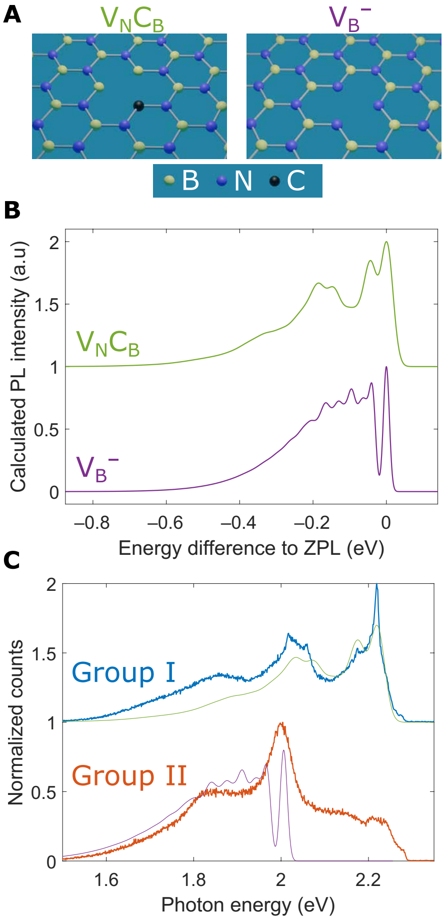

Fig. 5. Comparison of PL line shapes to ab initio DFT calculations. (**A**) Schematics of the V_NC_B and the V_B^- defects. (**B**) Calculated PL line shapes of V_NC_B and V_B^-. (**C**) Comparison of calculated and experimental PL line shapes obtained after 10-s irradiation at 240 eV and subsequent annealing. The calculated PL line shapes are shifted to the ZPL of each emitter and rescaled. The colors of the spectra in (B) correspond to the ones in (C).

photophysical properties similar to previously reported quantum emitters in hBN. We propose that both groups of luminescent centers are formed by amorphization of hBN via irradiation, followed by recrystallization via annealing where the luminescent centers are created in the topmost layers. This mechanism of generating luminescent centers highlights the necessity of both irradiation and annealing, confirmed by experimental findings. Furthermore, the proposed mechanism of generating luminescent centers is strongly supported by MD simulations of oxygen irradiation of hBN as well as experimental observations of bulk-phonon assisted PL. All in all, the combination of experimental and theoretical findings allows us to rule out defects unlikely to be formed during our process and to focus on the most likely defects to understand the microscopic origin of our luminescent centers. Ab initio calculations of PL line shapes show excellent agreement of group I centers with V_NC_B and of group II centers with V_B^-. Our comparison is qualitative and further spectroscopic methods would be needed to unambiguously identify the nature of these luminescent centers (*43*–*45*). Nevertheless, our excellent agreement of experimental and theoretical PL line shapes is outstanding compared to previous reports.

Our irradiation-based method relies on inexpensive and widely used equipment and therefore enables low-cost and large-scale generation of luminescent centers in hBN with controlled densities. Site-selective quantum emission at room temperature might be achieved by combining our depth-selective generation of luminescent centers with standard nanolithographic techniques. Furthermore, the irradiation engineering presented in this work could be adapted to other gapped 2D materials for generating typical defects such as vacancies or substitutional defects based on impurities intrinsic to the 2D material itself or originating from the annealing environment. Different irradiation energies and fluences, as well as different annealing environments, might be required to optimize the density of these typical defects, which could be known or even previously unknown types of quantum emitters.

MATERIALS AND METHODS

Sample fabrication

We used bulk hBN crystals from HQGraphene and mechanically exfoliated them with tape (low-adhesion release and ultraviolet release tape, EPL BT-150E-KL, Nitto Denko) onto a SiO_2/Si chip with an oxide thickness of ~100 nm. The chip was priorly rinsed in acetone and isopropyl alcohol (IPA), as well as oxygen plasma ashed for 5 min. The area of each hBN flake was determined by counting the number of pixels in the PL map showing the Raman-active E_{2g} phonon of hBN at 1366 cm^{-1} (*14*). Multiplying this number of pixels by the pixel area gives the area of each hBN flake with a precision of 5 μm^2. By their optical contrast with respect to the substrate, we could estimate a thickness range from 3 to 64 nm after irradiation. We note that irradiation is thinning out the flakes slightly (see section SXV), as observed for oxygen plasma treatment (*46*).

Afterward, the exfoliated hBN flakes were irradiated with oxygen atoms in an RIE reactor with parallel plate geometry. A high-frequency generator operating at 13.56 MHz is capacitively coupled to the bottom electrode. We use O_2 inlet gas at a constant flow of 40 sccm. The pressure in the reactor during the process is kept low at 30 mTorr to minimize the angular dispersion of the ions. Ions in the generated plasma acquire a kinetic energy $E_{kin} = qV_{DC}$ given by the ion charge q and the DC bias V_{DC} [sum of the DC self-bias, the main contribution, and the plasma potential; (*47*)]. Because of the composition of our plasma (see section SXII), we assume $q = 1$, as well as irradiation with mainly neutral oxygen atoms and a small contribution of positively charged oxygen. Furthermore, the irradiation is carried out in the collisionless regime (or close to it) since the mean-free path of oxygen ions in plasma is 1 cm (*48*) which is similar to the plate separation in our RIE reactor but larger than the sheath thickness for oxygen ions at our working pressure (*49*, *50*). This collisionless regime ensures a narrow energy distribution as well as a small angular dispersion, thus making our process well controlled and easy to model.

Our samples were irradiated at different kinetic energies by running processes at various V_{DC} = 120, 200, 240, 270, and 300 V. We measured fluctuations of V_{DC} in our reactor during the processes below ±5 V.

Two batches (batch 1 and batch 2) are used for studying different irradiation energies. Here, the irradiation time is kept constant at 10 s, which results in a fluence of 1×10^{14} to 1×10^{15} atoms/cm^2. One batch (batch 3) is used to study the irradiation fluence. Here, the irradiation time varies from 100 to 1000 s, resulting in fluences from 1×10^{15} to 1×10^{16} atoms/cm^2 to 1×10^{16} to 1×10^{17} atoms/cm^2.

Subsequently, the chips were annealed inside a graphite box at 850 °C in nitrogen (99.999%) for 30 min with a ramp of 20 °C/min for heating and cooling. The pressure in the chamber was 80 mbar when cold and 170 mbar when hot.

Optical spectroscopy

All PL measurements were performed with a customized scanning microscopy setup (details in section SI). All spectra are obtained at room temperature and are shown without background correction. All PL maps and spectra shown in Fig. 1, 3, and 5 are obtained with a 2.37-eV laser except the blue spectra for 240 and 270 eV in Fig. 3A where a 2.40-eV laser was used. The $g^{(2)}$ measurements in Fig. 3B were carried out with a 2.37-eV laser for samples irradiated at 200 eV and with a 2.40-eV laser for irradiation at 240 and 270 eV.

DFT calculations of PL line shapes

For our calculations of PL spectra of V_NC_B and V_B^- defects, the planar configurations of ground and excited states involved in the transitions were considered. While the planar configuration is the most stable one for all other cases, only for the excited state of V_NC_B (i.e., 2^3B_1) does the carbon atom of the defect relax out of plane. The out-of-plane configuration is stable compared to the planar configuration by 0.23 eV for monolayer hBN, while the energies differ by 0.036 eV in a trilayer hBN with a V_NC_B defect embedded in the central hBN layer. A very small barrier of 0.036 eV for trilayer hBN is consistent with the fact that only the planar configuration has a very good qualitative agreement with experimental PL spectra.

We used DFT calculations using HSE06 for exchange and correlation, since the PBE functional fails for defect states (*51*). We implemented our calculations in version 5.3.3 of the Vienna Ab Initio Simulation Package (*52*, *53*) and the ΔSCF method described in (*20*, *54*). For the detailed theory and for details on the calculation of the PL line shapes, we refer to (*39*).

Molecular dynamic simulations

We used the LAMMPS computational package (*55*) and defined the interaction between B and N atoms with an ExTeP (*35*) and at small separations with the Ziegler-Biersack-Littmark potential (*56*).

SUPPLEMENTARY MATERIALS

Supplementary material for this article is available at http://advances.sciencemag.org/cgi/content/full/7/8/eabe7138/DC1

REFERENCES AND NOTES

1. J. L. O'Brien, A. Furusawa, J. Vučković, Photonic quantum technologies. *Nat. Photonics* **3**, 687–695 (2009).
2. D. Jaque, F. Vetrone, Luminescence nanothermometry. *Nanoscale* **4**, 4301–4326 (2012).
3. X.-L. Chu, S. Götzinger, V. Sandoghdar, A single molecule as a high-fidelity photon gun for producing intensity-squeezed light. *Nat. Photonics* **11**, 58–62 (2017).
4. H. Wang, Y.-M. He, T.-H. Chung, H. Hu, Y. Yu, S. Chen, X. Ding, M.-C. Chen, J. Qin, X. Yang, R.-Z. Liu, Z.-C. Duan, J.-P. Li, S. Gerhardt, K. Winkler, J. Jurkat, L.-J. Wang, N. Gregersen, Y.-H. Huo, Q. Dai, S. Yu, S. Höfling, C.-Y. Lu, J.-W. Pan, Towards optimal single-photon sources from polarized microcavities. *Nat. Photonics* **13**, 770–775 (2019).
5. C. Kurtsiefer, S. Mayer, P. Zarda, H. Weinfurter, Stable solid-state source of single photons. *Phys. Rev. Lett.* **85**, 290–293 (2000).
6. C. Hepp, T. Müller, V. Waselowski, J. N. Becker, B. Pingault, H. Sternschulte, D. Steinmüller-Nethl, A. Gali, J. R. Maze, M. Atatüre, C. Becher, Electronic structure of the silicon vacancy color center in diamond. *Phys. Rev. Lett.* **112**, 036405 (2014).
7. A. Srivastava, M. Sidler, A. V. Allain, D. S. Lembke, A. Kis, A. Imamoğlu, Optically active quantum dots in monolayer WSe_2. *Nat. Nanotechnol.* **10**, 491–496 (2015).
8. M. Koperski, K. Nogajewski, A. Arora, V. Cherkez, P. Mallet, J.-Y. Veuillen, J. Marcus, P. Kossacki, M. Potemski, Single photon emitters in exfoliated WSe_2 structures. *Nat. Nanotechnol.* **10**, 503–506 (2015).
9. Y.-M. He, G. Clark, J. R. Schaibley, Y. He, M.-C. Chen, Y.-J. Wei, X. Ding, Q. Zhang, W. Yao, X. Xu, C.-Y. Lu, J.-W. Pan, Single quantum emitters in monolayer semiconductors. *Nat. Nanotechnol.* **10**, 497–502 (2015).
10. J. Klein, M. Lorke, M. Florian, F. Sigger, L. Sigl, S. Rey, J. Wierzbowski, J. Cerne, K. Müller, E. Mitterreiter, P. Zimmermann, T. Taniguchi, K. Watanabe, U. Wurstbauer, M. Kaniber, M. Knap, R. Schmidt, J. J. Finley, A. W. Holleitner, Site-selectively generated photon emitters in monolayer MoS_2 via local helium ion irradiation. *Nat. Commun.* **10**, 2755 (2019).
11. M. Pelton, Modified spontaneous emission in nanophotonic structures. *Nat. Photonics* **9**, 427–435 (2015).
12. I. Aharonovich, D. Englund, M. Toth, Solid-state single-photon emitters. *Nat. Photonics* **10**, 631–641 (2016).
13. G. Cassabois, P. Valvin, B. Gil, Hexagonal boron nitride is an indirect bandgap semiconductor. *Nat. Photonics* **10**, 262–266 (2016).
14. T. T. Tran, K. Bray, M. J. Ford, M. Toth, I. Aharonovich, Quantum emission from hexagonal boron nitride monolayers. *Nat. Nanotechnol.* **11**, 37–41 (2016).
15. T. Vogl, R. Lecamwasam, B. C. Buchler, Y. Lu, P. K. Lam, Compact cavity-enhanced single-photon generation with hexagonal boron nitride. *ACS Photonics* **6**, 1955–1962 (2019).
16. N. V. Proscia, R. J. Collison, C. A. Meriles, V. M. Menon, Coupling of deterministically activated quantum emitters in hexagonal boron nitride to plasmonic surface lattice resonances. *Nanophotonics* **8**, 2057–2064 (2019).
17. I. Aharonovich, M. Toth, Quantum emitters in two dimensions. *Science* **358**, 170–171 (2017).
18. M. K. Boll, I. P. Radko, A. Huck, U. L. Andersen, Photophysics of quantum emitters in hexagonal boronnitride nano-flakes. *Opt. Express* **28**, 7475–7487 (2020).
19. F. Hayee, L. Yu, J. L. Zhang, C. J. Ciccarino, M. Nguyen, A. F. Marshall, I. Aharonovich, J. Vučković, P. Narang, T. F. Heinz, J. A. Dionne, Revealing multiple classes of stable quantum emitters in hexagonal boron nitride with correlated optical and electron microscopy. *Nat. Mater.* **19**, 534–539 (2020).
20. S. A. Tawfik, A. Sajid, M. Fronzi, M. Kianinia, T. T. Tran, C. Stampfl, I. Aharonovich, M. Toth, M. J. Ford, First-principles investigation of quantum emission from hBN defects. *Nanoscale* **9**, 13575–13582 (2017).
21. L. Weston, D. Wickramaratne, M. Mackoit, A. Alkauskas, C. G. Van de Walle, Native point defects and impurities in hexagonal boron nitride. *Phys. Rev. B* **97**, 214104 (2018).
22. C. Linderälv, W. Wieczorek, P. Erhart, Vibrational signatures for the identification of single-photon emitters in hexagonal boron nitride. arXiv:2008.05817 [cond-mat.mtrl-sci] (2020).
23. T. T. Tran, C. Elbadawi, D. Totonjian, C. J. Lobo, G. Grosso, H. Moon, D. R. Englund, M. J. Ford, I. Aharonovich, M. Toth, Robust multicolor single photon emission from point defects in hexagonal boron nitride. *ACS Nano* **10**, 7331–7338 (2016).
24. T. Vogl, G. Campbell, B. C. Buchler, Y. Lu, P. K. Lam, Fabrication and deterministic transfer of high-quality quantum emitters in hexagonal boron nitride. *ACS Photonics* **5**, 2305–2312 (2018).
25. Z.-Q. Xu, C. Elbadawi, T. T. Tran, M. Kianinia, X. Li, D. Liu, T. B. Hoffman, M. Nguyen, S. Kim, J. H. Edgar, X. Wu, L. Song, A. Sajid, M. Ford, M. Toth, I. Aharonovich, Single photon emission from plasma treated 2D hexagonal boron nitride. *Nanoscale* **10**, 7957–7965 (2018).
26. S. Choi, T. T. Tran, C. Elbadawi, C. Lobo, X. Wang, S. Juodkazis, G. Seniutinas, M. Toth, I. Aharonovich, Engineering and localization of quantum emitters in large hexagonal boron nitride layers. *ACS Appl. Mater. Interfaces* **8**, 29642–29648 (2016).
27. N. Mendelson, D. Chugh, J. R. Reimers, T. S. Cheng, A. Gottscholl, H. Long, C. J. Mellor, A. Zettl, V. Dyakonov, P. H. Beton, S. V. Novikov, C. Jagadish, H. H. Tan, M. J. Ford, M. Toth, C. Bradac, I. Aharonovich, Identifying carbon as the source of visible single-photon emission from hexagonal boron nitride. *Nat. Mater.* , (2020).
28. A. V. Krasheninnikov, F. Banhart, Engineering of nanostructured carbon materials with electron or ion beams. *Nat. Mater.* **6**, 723–733 (2007).
29. I. Lin, D. C. Hinson, W. H. Class, R. L. Sandstrom, Low-energy high flux reactive ion etching by rf magnetron plasma. *Appl. Phys. Lett.* **44**, 185–185 (1984).
30. S. Reich, A. C. Ferrari, R. Arenal, A. Loiseau, I. Bello, J. Robertson, Resonant Raman scattering in cubic and hexagonal boron nitride. *Phys. Rev. B* **71**, 205201 (2005).
31. M. A. Feldman, A. Puretzky, L. Lindsay, E. Tucker, D. P. Briggs, P. G. Evans, R. F. Haglund, B. J. Lawrie, Phonon-induced multicolor correlations in hBN single-photon emitters. *Phys. Rev. B* **99**, 020101 (2019).
32. G. Grosso, H. Moon, C. J. Ciccarino, J. Flick, N. Mendelson, L. Mennel, M. Toth, I. Aharonovich, P. Narang, D. R. Englund, Low-temperature electron–phonon interaction of quantum emitters in hexagonal boron nitride. *ACS Photonics* **7**, 1410–1417 (2020).
33. X. Li, G. D. Shepard, A. Cupo, N. Camporeale, K. Shayan, Y. Luo, V. Meunier, S. Strauf, Nonmagnetic quantum emitters in boron nitride with ultranarrow and sideband-free emission spectra. *ACS Nano* **11**, 6652–6660 (2017).
34. P. Grünwald, Effective second-order correlation function and single-photon detection. *New J. Phys.* **21**, 093003 (2019).
35. J. H. Los, J. M. H. Kroes, K. Albe, R. M. Gordillo, M. I. Katsnelson, A. Fasolino, Extended Tersoff potential for boron nitride: Energetics and elastic properties of pristine and defective *h*-BN. *Phys. Rev. B* **96**, 184108 (2017).
36. O. L. Krivanek, M. F. Chisholm, V. Nicolosi, T. J. Pennycook, G. J. Corbin, N. Dellby, M. F. Murfitt, C. S. Own, Z. S. Szilagyi, M. P. Oxley, S. T. Pantelides, S. J. Pennycook, Atom-by-atom structural and chemical analysis by annular dark-field electron microscopy. *Nature* **464**, 571–574 (2010).
37. X. Wei, M.-S. Wang, Y. Bando, D. Golberg, Electron-beam-induced substitutional carbon doping of boron nitride nanosheets, nanoribbons, and nanotubes. *ACS Nano* **5**, 2916–2922 (2011).
38. B. Huang, H. Lee, Defect and impurity properties of hexagonal boron nitride: A first-principles calculation. *Phys. Rev. B* **86**, 245406 (2012).
39. A. Sajid, K. S. Thygesen, V_NC_B defect as source of single photon emission from hexagonal boron nitride. *2D Mater.* **7**, 031007 (2020).
40. A. Sajid, K. S. Thygesen, J. R. Reimers, M. J. Ford, Edge effects on optically detected magnetic resonance of vacancy defects in hexagonal boron nitride. *Commun. Phys.* **3**, 153 (2020).
41. A. Gottscholl, M. Kianinia, V. Soltamov, S. Orlinskii, G. Mamin, C. Bradac, C. Kasper, K. Krambrock, A. Sperlich, M. Toth, I. Aharonovich, V. Dyakonov, Initialization and read-out of intrinsic spin defects in a van der Waals crystal at room temperature. *Nat. Mater.* **19**, 540–545 (2020).
42. A. Sajid, M. J. Ford, J. R. Reimers, Single-photon emitters in hexagonal boron nitride: A review of progress. *Rep. Prog. Phys.* **83**, 044501 (2020).
43. N. Alem, O. V. Yazyev, C. Kisielowski, P. Denes, U. Dahmen, P. Hartel, M. Haider, M. Bischoff, B. Jiang, S. G. Louie, A. Zettl, Probing the out-of-plane distortion of single point defects in atomically thin hexagonal boron nitride at the picometer scale. *Phys. Rev. Lett.* **106**, 126102 (2011).
44. D. Wong, J. Velasco Jr., L. Ju, J. Lee, S. Kahn, H.-Z. Tsai, C. Germany, T. Taniguchi, K. Watanabe, A. Zettl, F. Wang, M. F. Crommie, Characterization and manipulation of individual defects in insulating hexagonal boron nitride using scanning tunnelling microscopy. *Nat. Nanotechnol.* **10**, 949–953 (2015).
45. N. Alem, R. Erni, C. Kisielowski, M. D. Rossell, W. Gannett, A. Zettl, Atomically thin hexagonal boron nitride probed by ultrahigh-resolution transmission electron microscopy. *Phys. Rev. B* **80**, 155425 (2009).
46. T. Vogl, M. W. Doherty, B. C. Buchler, Y. Lu, P. K. Lam, Atomic localization of quantum emitters in multilayer hexagonal boron nitride. *Nanoscale* **11**, 14362–14371 (2019).
47. M. Wojtaszek, N. Tombros, A. Caretta, P. H. M. van Loosdrecht, B. J. van Wees, A road to hydrogenating graphene by a reactive ion etching plasma. *J. Appl. Phys.* **110**, 063715 (2011).
48. P. K. Chu, S. Qin, C. Chan, N. W. Cheung, P. K. Ko, Instrumental and process considerations for the fabrication of silicon-on-insulators (soi) structures by plasma immersion ion implantation. *IEEE Trans. Plasma Sci.* **26**, 79–84 (1998).
49. K. Dittmann, "Detailed investigations of the sheath dynamics and elementary processes in capacitively coupled rf plasmas," thesis, University of Greifswald (2009).
50. N. Mutsukura, K. Kobayashi, Y. Machi, Plasma sheath thickness in radio-frequency discharges. *J. Appl. Phys.* **68**, 2657–2660 (1990).

51. J. R. Reimers, A. Sajid, R. Kobayashi, M. J. Ford, Understanding and calibrating density-functional-theory calculations describing the energy and spectroscopy of defect sites in hexagonal boron nitride. *J. Chem. Theory Comput.* **14**, 1602–1613 (2018).
52. G. Kresse, J. Hafner, *Ab initio* molecular dynamics for liquid metals. *Phys. Rev. B* **47**, 558–561 (1993).
53. G. Kresse, J. Furthmüller, Efficiency of ab-initio total energy calculations for metals and semiconductors using a plane-wave basis set. *Comput. Mater. Sci.* **6**, 15–50 (1996).
54. A. Sajid, J. R. Reimers, M. J. Ford, Defect states in hexagonal boron nitride: Assignments of observed properties and prediction of properties relevant to quantum computation. *Phys. Rev. B* **97**, 064101 (2018).
55. S. Plimpton, Fast parallel algorithms for short-range molecular dynamics. *J. Comput. Phys.* **117**, 1–19 (1995).
56. J. Ziegler, J. Biersack, U. Littmark, *The Stopping and Range of Ions in Solids* (Pergamon Press, 1985), vol. 1, p. 321.

Acknowledgments: We thank D. I. Miakota and S. Canulescu for help with thermal annealing. F. Sterl helped with creating the illustrations of our process in Fig. 1A. **Funding:** This work was funded by the Danish National Research Foundation through the Center for Nanostructured Graphene (grant number DNRF103) and through NanoPhoton - Center for Nanophotonics (grant number DNRF147). N.S. acknowledges support from VILLUM FONDEN (grant no. 00028233). M.W. and N.S. acknowledge support from the Independent Research Fund Denmark - Natural Sciences (project no. 0135-004038). J.M.C. acknowledges support from Vinnova (grant no. 2019-02878) and MINECO Ramón y Cajal program (project no. RYC2019-028443-I). S.X. acknowledges the support from Independent Research Fund Denmark (project no. 9041-00333B). J.M.C., L.G., and P.B. acknowledge the support from EU H2020 Graphene Flagship, grant agreements 785219 (Core 2) and 881603 (Core 3). A.S. and K.S.T. acknowledge the support from the European Research Council (ERC) under the European Union's Horizon 2020 research and innovation program (grant no. 773122, LIMA). A.V.K. acknowledges the financial support of the Deutsche Forschungsgemeinschaft (DFG) through project KR 4866/2-1. Parts of our optical setup are financed through the IDUN Center of Excellence funded by the Danish National Research Foundation (project no. DNRF122) and VILLUM FONDEN (Grant No. 9301). **Author contributions:** M.F. carried out all experiments. M.F., J.M.C., and N.S. designed the experiments. M.F. and N.S. analyzed and interpreted the experimental data. A.S. contributed to the ab initio calculations of PL line shapes and was involved in the discussion of the experimental results. S.G., M.G.-A., and A.V.K. performed the MD simulations and band structure calculations. J.M.C. and L.G. carried out the irradiation. K.S.T. supervised the ab initio calculations of PL line shapes. S.X. and M.W. contributed to the discussion of the experimental results. M.F. and N.S. wrote the manuscript with input from all co-authors. All authors discussed the results and commented on the manuscript. **Competing interests:** The authors declare that they have no competing interests. **Data and materials availability:** All data needed to evaluate the conclusions in the paper are present in the paper and/or the Supplementary Materials. Additional data related to this paper may be requested from the authors.

Submitted 11 September 2020
Accepted 6 January 2021
Published 17 February 2021
10.1126/sciadv.abe7138

Citation: M. Fischer, J. M. Caridad, A. Sajid, S. Ghaderzadeh, M. Ghorbani-Asl, L. Gammelgaard, P. Bøggild, K. S. Thygesen, A. V. Krasheninnikov, S. Xiao, M. Wubs, N. Stenger, Controlled generation of luminescent centers in hexagonal boron nitride by irradiation engineering. *Sci. Adv.* **7**, eabe7138 (2021).

Science Advances

Controlled generation of luminescent centers in hexagonal boron nitride by irradiation engineering

M. Fischer, J. M. Caridad, A. Sajid, S. Ghaderzadeh, M. Ghorbani-Asl, L. Gammelgaard, P. Bøggild, K. S. Thygesen, A. V. Krasheninnikov, S. Xiao, M. Wubs, and N. Stenger

Sci. Adv. **7** (8), eabe7138. DOI: 10.1126/sciadv.abe7138

Science Advances (ISSN 2375-2548) is published by the American Association for the Advancement of Science. 1200 New York Avenue NW, Washington, DC 20005. The title *Science Advances* is a registered trademark of AAAS.